A&A 553, A114 (2013)
DOI: 10.1051/0004-6361/201220683

Astronomy & Astrophysics

Gas and dust cooling along the major axis of M 33 (`HerM33es`)

ISO/LWS [C ii] observations[⋆,⋆⋆]

C. Kramer[1], J. Abreu-Vicente[1], S. García-Burillo[2], M. Relaño[3], S. Aalto[4], M. Boquien[5], J. Braine[6], C. Buchbender[1], P. Gratier[6,7], F. P. Israel[8], T. Nikola[9], M. Röllig[10], S. Verley[3], P. van der Werf[8], and E. M. Xilouris[11]

[1] Instituto Radioastronomía Milimétrica (IRAM), Av. Divina Pastora 7, Nucleo Central, 18012 Granada, Spain
e-mail: kramer@iram.es
[2] Observatorio Astronómico Nacional (OAN) – Observatorio de Madrid, Alfonso XII 3, 28014 Madrid, Spain
[3] Departamento de Fisica Teórica y del Cosmos, Universidad de Granada, 18071 Granada, Spain
[4] Department of Radio and Space Science, Onsala Observatory, Chalmers University of Technology, 43992 Onsala, Sweden
[5] Aix Marseille Université, CNRS, LAM (Laboratoire d'Astrophysique de Marseille) UMR 7326, 13388 Marseille, France
[6] Laboratoire d'Astrophysique de Bordeaux, Observatoire de Bordeaux, 33270 Floirac, France
[7] IRAM, 300 rue de la Piscine, 38406 Saint-Martin d'Hères, France
[8] Leiden Observatory, Leiden University, PO Box 9513, 2300 RA Leiden, The Netherlands
[9] Department of Astronomy, Cornell University, Ithaca, NY 14853, USA
[10] KOSMA, I. Physikalisches Institut, Universität zu Köln, Zülpicher Straße 77, 50937 Köln, Germany
[11] Institute of Astronomy and Astrophysics, National Observatory of Athens, P. Penteli, 15236 Athens, Greece

Received 1 November 2012 / Accepted 29 March 2013

ABSTRACT

Aims. We aim to better understand the heating of gas by observing the prominent gas cooling line [C ii] at 158 μm in the low-metallicity environment of the Local Group spiral galaxy M 33 on scales of 280 pc. In particular, we describe the variation of the photoelectric heating efficiency with the galactic environment.

Methods. In this study, we present [C ii] observations along the major axis of M 33 using the Infrared Space Observatory in combination with *Herschel* continuum maps, IRAM 30 m CO 2–1, and VLA H i data to study the variation in velocity integrated intensities. The ratio of [C ii] emission over the far-infrared continuum is used as a proxy for the heating efficiency, and models of photon-dominated regions are used to study the local physical densities, far-ultraviolet radiation fields, and average column densities of the molecular clouds.

Results. The heating efficiency stays constant at 0.8% in the inner 4.5 kpc radius of the galaxy, where it increases to reach values of ∼3% in the outskirts at about a 6 kpc radial distance. The rise of efficiency is explained in the framework of PDR models by lowered volume densities and FUV fields for optical extinctions of only a few magnitudes at constant metallicity. For the significant fraction of H i emission stemming from PDRs and for typical pressures found in the Galactic cold neutral medium (CNM) traced by H i emission, the CNM contributes ∼15% to the observed [C ii] emission in the inner 2 kpc radius of M 33. The CNM contribution remains largely undetermined in the south, while positions between radial distances of 2 and 7.3 kpc in the north of M 33 show a contribution of ∼40% ± 20%.

Key words. galaxies: ISM – photon-dominated region (PDR) – ISM: structure – evolution

1. Introduction

In photon-dominated regions (PDRs), far-ultraviolet (FUV) photons from stars dominate the chemistry and the energy balance in the interstellar gas. All the atomic and a large part of the molecular hydrogen of the interstellar medium (ISM) are located in PDRs, which emit a large fraction of far infrared (FIR) and millimeter emission (Tielens & Hollenbach 1985; Bakes & Tielens 1994; Hollenbach & Tielens 1997).

The [C ii] FIR fine structure line at 157.7 μm is the most important gas coolant. The [O i] 63 μm fine structure line starts to dominate in denser and warmer regions, when densities exceed about 10^4 cm^{-3} (Röllig et al. 2006). The photoelectric effect provides one of the dominant gas heating processes in PDRs. FUV photons eject electrons from dust grains or polycyclic aromatic hydrocarbon (PAH) molecules, heating the gas with their kinetic energy. Theoretical models have predicted efficiencies $\epsilon_{\rm PE}$ of up to a few percent (Weingartner & Draine 2001), consistent with observations. The ratio of emerging [C ii] intensity over the infrared continuum radiated by the dust has often been used as a measure of this efficiency. Observations of clouds in the Milky Way show variations over more than 2 orders of magnitude, between 10^{-4} and 3×10^{-2} (e.g. Vastel et al. 2001; Habart et al. 2001; Mizutani et al. 2004; Jakob et al. 2007). A similar variation is found in observations of external galaxies (e.g. Malhotra et al. 2001; Rubin et al. 2009). The scatter has been attributed to changes in the mean charge of small grains and PAHs (Okada et al. 2013). However, the change of $\epsilon_{\rm PE}$ in low-metallicity environments, such as those encountered in the

---

[⋆] *Herschel* is an ESA space observatory with science instruments provided by European-led PrincipalInvestigator consortia and with important participation from NASA.

[⋆⋆] Appendices are available in electronic form at `http://www.aanda.org`

Table 1. Observation Log of all [C II] observations of ISO/LWS along the major axis of M 33.

IDA name	Abbrev.^{a}	TDT^b (Obs. #ID)	RA^c	Dec.^{c}	Observer ID	Ref.	Type	AOT
M 33S2	S2	59901107	01h33m08.5s	+30d17m00.0s	KMOCHIZU	–	Raster	LO2
M 33S	S1	78600403	01h33m37.1s	+30d31m34.7s	KMOCHIZU	(1)	Raster	LO2
M 33 Nucleus		80800367	01h33m50.9s	+30d39m36.8s	HSMITH	(1, 2)	Point	LO2
M 33N	N1	78600801	01h34m07.3s	+30d46m55.7s	KMOCHIZU	–	Raster	LO2
M 33N2	N2	59900605	01h34m36.3s	+31d01m29.2s	KMOCHIZU	–	Raster	LO2

Notes. $^{(a)}$ Abbreviation used in the text. $^{(b)}$ Target Dedicated Time. $^{(c)}$ The given coordinates are the central position of each raster strip of 19 positions.

References. (1) Brauher et al. (2008); (2) Higdon et al. (2003).

Magellanic Clouds or M 33, is not yet well understood (e.g. Israel & Maloney 2011). Interestingly, the efficiency drops for local ultra-luminous infrared galaxies (ULIRGs; Luhman et al. 2003; Graciá-Carpio et al. 2011) and for some ULIRGs at high redshifts (e.g. Stacey et al. 2010; Cox et al. 2011).

M 33 is a nearby galaxy located at 840 kpc distance (Freedman et al. 1991). Its overall metallicity is about half-solar (Magrini et al. 2010), which is only slightly higher than that of the Large Magellanic Cloud (LMC; Hunter et al. 2007). M 33 is an Sc galaxy which exhibits a prominent, flocculent spiral structure together with an underlying extended diffuse component. This structure is seen in the 250 μm map of M 33 which was observed in the framework of the *Herschel* open time key project `HerM33es` (Kramer et al. 2010) (Fig. 1). M 33 has a moderate inclination of 56°, which allows studies of the ISM at a low depth along the line-of-sight. Its proximity allows high spatial resolution studies.

While previous studies have only discussed [C II] emission at a few selected positions in M 33, there have been no systematic studies that describe the spatial variation of [C II] emission in the disk of the galaxy. Higdon et al. (2003) used ISO/LWS[1] to study [C II] other FIR emission lines, and the continuum in the nucleus and in six H II regions. They found [C II]/FIR$_{\rm LWS}$ values between 0.2% and 0.7%. Brauher et al. (2008) compiled ISO/LWS data of 227 galaxies, which included 23 positions in M 33 with [C II] data. Plotting the [C II]/FIR ratio for all galaxies, they find variations from 10^{-4} to greater than 1%. Mookerjea et al. (2011) and Braine et al. (2012) analyzed the first *Herschel*/PACS and HIFI spectroscopic data sets of the `HerM33es` project. They found [C II]/FIR ratios between 0.01% and 2% in a 2′ × 2′ box centered on the BCLMP 302 H II region, and a ratio of 1.1% at the position of the BCLMP 691 H II region that lies at galacto-centric distances of 2.1 and 3.3 kpc, respectively, along the major axis.

In this paper, we present archival ISO/LWS [C II] data along the major axis of M 33 up to a galacto-centric distance of 8 kpc. We study the radial distributions and correlations among [C II], the FIR continuum, CO, H I, and Hα. We also study the radial distribution of the [C II]/FIR ratio. We compare the observations in M 33 with data of star-forming regions in the Milky Way with other external galaxies including low-metallicity objects. Local volume densities and FUV fields of the [C II] and CO emitting gas are estimated using the Kaufman et al. (1999, K99) PDR model. The observed [C II] emission is also compared with an estimate of the [C II] emission emitted by atomic clouds.

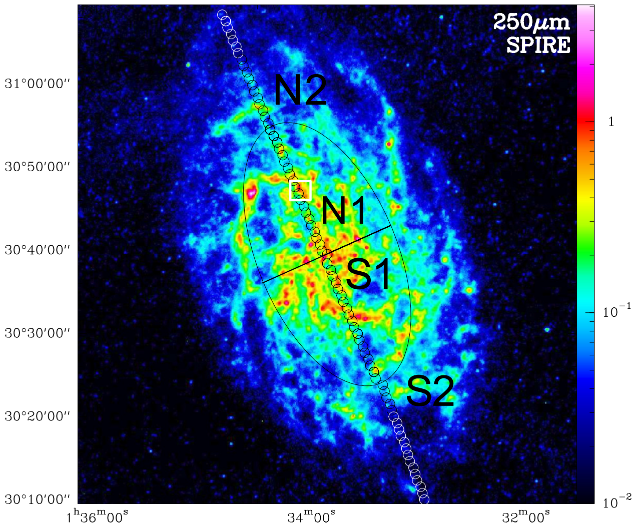

Fig. 1. *Herschel* SPIRE 250 μm map of M 33 (Xilouris et al. 2012). Units are Jy/(18″ beam). Circles mark the position and beam size of the ISO/LWS [C II] observations along the major axis of M 33. The ellipse delineates the galacto-centric distance of 4.5 kpc, which devides the observed inner (N1 and S1) and outer (N2 and S2) regions. The white square marks the BCLMP 302 H II region. Coordinates are RA and Dec. (Eq. J2000).

2. Observations and data analysis

2.1. [C II] 158 μm (ISO/LWS)

We list all ISO/LWS [C II] spectra observed along the major axis of M 33 at a position angle of 23° in Table 1. The spectra were observed using the partial grating scan mode (LWS AOT[2] LO2). This AOT covers the wavelength range 43−196.9 μm, and it has a medium spectral resolution of $\Delta\lambda/\lambda \sim 200$ which corresponds to 1500 km s^{-1} at the wavelength of the [C II] line. The LWS flux-calibration and its relative spectral response function were derived from observations of Uranus (Swinyard et al. 1998). The angular resolution is 69.4″ (Gry et al. 2003) which corresponds to a linear resolution of 280 pc. The spectra have been automatically processed by the ISO system. We retrieved spectra at 77 positions from the ISO Data Archive (IDA) for further processing. The observed positions cover about ± 8 kpc (±33′) from the nucleus on a grid of about 208 pc (Fig. 1).

We averaged the observations at each position, subtracted linear baselines, and fitted a Gaussian to the line. Data were analyzed using the ISO Spectral Analysis Package (ISAP v2.1 Sturm et al. 1998). We assume a calibration error of 15%

---

[1] Infrared Space Observatory (Kessler et al. 1996)/Long-Wave Spectrometer (Gry et al. 2003).

[2] Astronomical Observing Template.

(Higdon et al. 2003). Some sample spectra are shown in Appendix C.

Figure 2 shows the variation of [C II] intensities along the major axis. [C II] is detected above 3σ at 36 positions. Stacking of the neighboring positions increased the number of detections. Tables A.1 and A.2 in the Appendix list the stacked positions.

2.2. Far-infrared continuum

To measure the total FIR continuum, we combined SPIRE and PACS maps of M 33 at five wavelengths between 500 and 100 μm (Boquien et al. 2011; Xilouris et al. 2012), which are taken in the framework of `HerM33es` with MIPS/*Spitzer* 24 and 70 μm maps (Verley et al. 2007; Tabatabaei et al. 2007). These maps were smoothed to the ISO/LWS resolution using Gaussian kernels. The fluxes were extracted using circular apertures of 69.4″ centered at the ISO/LWS positions. A two-component greybody function was fitted to the spectral energy distribution (SED) at each position, following the method described in Kramer et al. (2010). Integrating between 42.5 μm and 122.5 μm (Dale & Helou 2002) yields the FIR surface brightness. The dust emissivity index β was fixed at 1.5, which was found to be the best-fitting value for M 33 (Kramer et al. 2010; Xilouris et al. 2012). The total FIR luminosity is, however, robust against changes of β. Figure 2 shows the variation of relative FIR intensities along the major axis (cf. Table B.1). A few sample SEDs are shown in Appendix C. We also integrated the fitted SEDs over the range 3−1000 μm wavelengths to estimate total infrared (TIR) intensities (Dale & Helou 2002), thereby deriving the ratios between TIR over FIR, which lie between 2.7 and 1.3 (Table B.1).

2.3. CO, H*I*, Hα

Complementary CO and H I data were used as tracers of the molecular gas and the atomic gas to compare with [C II] emission. The CO 2−1 line was mapped with the IRAM 30m telescope by Gardan et al. (2007) and Gratier et al. (2010). These maps cover the major axis up to a distance of 8.5 kpc in the north and 6.5 kpc in the south. The CO map covers all ISO/LWS [C II] positions, except for the eight southernmost positions.

We determined 3σ upper limits of the integrated intensities using $\sigma = \sqrt{N}\Delta v_{\rm res}\, T_{\rm mb}^{\rm rms}$ where the number of channels is defined as N over the velocity extent of the line, the velocity resolution $\Delta v_{\rm res}$, and corresponding baseline rms $T_{\rm mb}^{\rm rms}$. The H I VLA map of M 33 (Gratier et al. 2010) covers the entire galaxy up to 8.5 kpc radial distance. H I is detected at all ISO/LWS positions. While no single dish data were combined with the interferometric observations, the total flux recovered over the entire galaxy by the interferometric observations alone corresponds to more than 90% of the flux measured at the Arecibo single dish telescope (Putman et al. 2009).

We also used a map of Hα emission presented in Hoopes & Walterbos (2000) and by Verley et al. (2007). These data were obtained at the 0.6 m Burrell-Schmidt telescope at Kitt Peak National Observatory (KPNO). Hα is detected at 42 ISO/LWS positions.

Intensities have been calculated by smoothing all data to the angular resolution of the LWS [C II] data, as described in the Appendix B. The variation of relative intensities of CO, H I, and Hα is shown in Fig. 2, and absolute intensities are listed in Table B.1. We stacked CO, H I, and Hα over the same positions as [C II] (cf. Tables A.1, A.2).

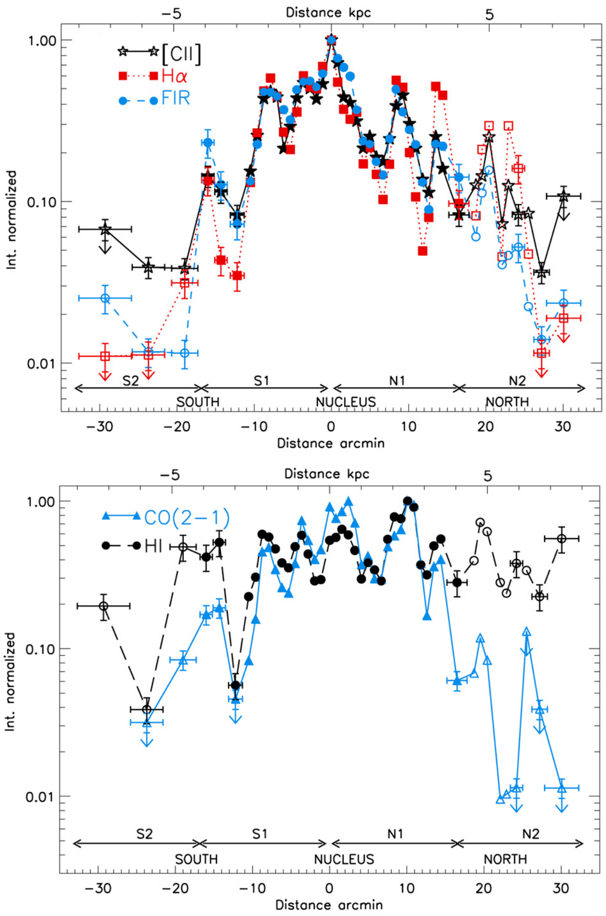

Fig. 2. Normalized integrated intensities of [C II], FIR, Hα, CO 2−1, and H I along the major axis of M 33. Closed symbols show data within 4.5 kpc of the nucleus (N1, S1), and open symbols show observations in the outer galaxy (N2, S2). Horizontal errorbars show the region over which different [C II] spectra from neighboring positions were averaged.

3. Results

3.1. Correlation among [C*II*], FIR, Hα, CO, and H*I*

The emission of [C II], the FIR continuum, and Hα are all well correlated along the major axis, especially in the inner 10′ (Fig. 2). These tracers of star formation all peak at the nucleus and drop by more than one order of magnitude beyond ~20′ radial distance. Closer inspection shows that the FIR continuum drops more steeply than [C II], which is discussed further below. In general, [C II], FIR, and Hα however all trace the spiral arms and the inter-arm regions. The close correlation is even more clearly seen in Fig. 3, where we plot the various tracers against [C II] emission. A close correlation of [C II] with other tracers of star formation is well-known for other sources and has also been seen in the ISO/LWS maps, which are a portion of the northern arm of M 31 by Rodriguez-Fernandez et al. (2006).

The atomic and molecular gas traced by H I and CO also drops with radial distance. However, the drop is much steeper for CO than for H I (Fig. 2). In the inner part of the galaxy that is within 10′ radial distance, the distribution of CO and H I is rather flat, which contrasts to that of the FIR continuum. The distribution of emission of both gas tracers is not symmetrical with respect to the nucleus. Instead, CO and H I peak near 10′ (~2.5 kpc) to the north and only show a secondary maximum at the nucleus. The absolute maximum corresponds to GMC 91

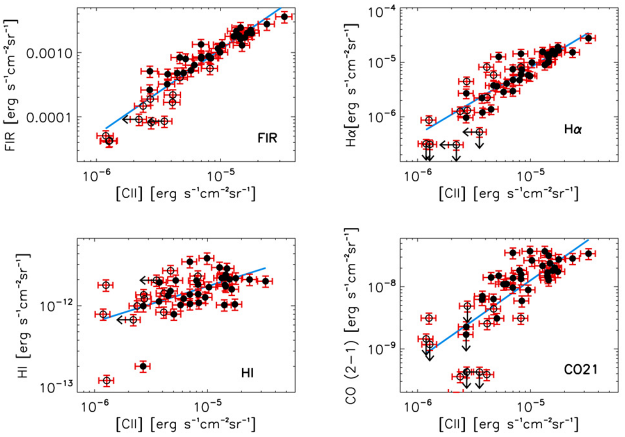

Fig. 3. Correlation of [C II] intensities of the FIR continuum, Hα emission, CO, and H I in double-logarithmic plots. All intensities are given in units of erg s^{-1} cm^{-2} sr^{-1}. Straight lines delineate the results of linear least-squares fits to the data. Closed and open symbols distinguish between positions in the inner (S1, N1) and outer (S2, N2) disk of M 33, respectively.

Table 2. Linear least-squares fits of the correlations of [C II], FIR, Hα, CO, and H I (cf. Fig. 3) in the form log FIR= $a + b$ log [C II] with correlation coefficients r.

	FIR-[C II]	Hα-[C II]	CO(2−1)-[C II]	H I-[C II]
a	3.71	1.08	−1.52	−9.74
b	1.33	1.23	1.27	0.41
r	0.90	0.79	0.59	0.30

(Engargiola et al. 2003; Gratier et al. 2010; Buchbender et al. 2013) and to cloud 245 in Gratier et al. (2012).

Figure 3 shows correlations of [C II] emission, FIR, Hα, CO, and H I. Linear fits are weighted by the error along both axes, which we assume to be 15% for [C II] and H I and 20% for CO and the FIR continuum. The fits confirm that [C II] is strongly correlated with FIR and Hα using the linear correlation coefficients (r) 0.90 and 0.79, respectively (Table 2). In contrast, the correlation with CO is much weaker where $r = 0.59$, and very poor for H I where $r = 0.30$. This result confirms that [C II] is a good tracer of the star formation rate at the ISO/LWS beam size scale. Points from the northern most region N2 deviate slightly from the fit both in the [C II]-FIR and the [C II]-Hα plots which shows a worse correlation between [C II] and star-forming tracers in the northern outer galaxy.

3.2. Radial variation of intensity ratios

The radial distributions of the ratios [C II]/CO 1−0, FIR/CO 1−0 and H I/CO 1−0 are shown in Fig. 4. We estimated CO 1−0 intensities from the CO 2−1 line (cf. Appendix B). All three ratios show a minimum in the inner part of the galaxy and an increase towards the outer part. This observation reflects the steep drop of CO intensities already seen in the radial distribution of intensities (Fig. 2). The H I/CO ratio shows a minimum near the nucleus and rises steadily towards the outskirts over about two orders of magnitude. While this behavior is nearly symmetrical in the north and south of the galaxy, this symmetry is broken for the [C II]/CO and FIR/CO ratios. The latter two ratios show a minimum at about 10′ to the north near GMC 91 where the CO emission peaks (Fig. 2). To the south of this minimum, the two ratios steadily increase. Towards the north, the two ratios also increases but with more scatter.

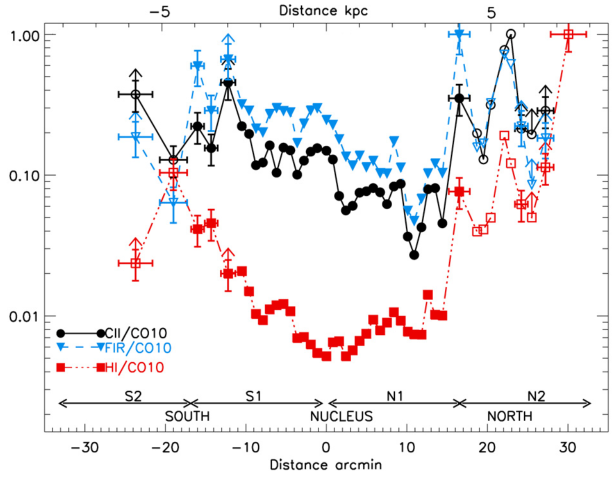

Fig. 4. Normalized radial distributions of the [C II]/CO 1−0, FIR/CO 1−0, and H I/CO 1−0 intensity ratios on the erg-scale.

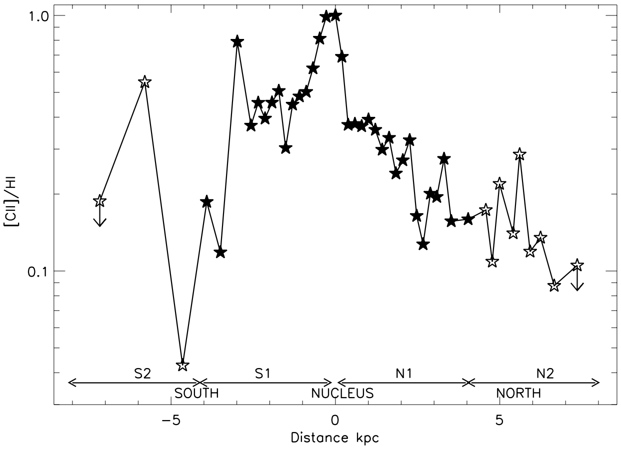

Fig. 5. Normalized radial distribution of the [C II]/H I intensity ratio.

In general, the [C II] emission drops more steeply with galacto-centric radius than the H I emission. This drop is most clearly seen in the northern part of the strip (Fig. 5). In contrast, the southern outer disk shows strongly varying [C II]/H I ratios which owe to the strong variability of H I emission (cf. Fig. 2).

3.3. [CII] /FIR ratio

In the inner part of the galaxy (N1, S1), the [C II]/FIR ratio stays constant at about 0.8% ± 0.2% (Fig. 6) but rises significantly and steeply in the outskirts to values of ~3%. The rise of the [C II]/FIR ratio is caused by the steep drop of FIR emission relative to the [C II] (Fig. 2) which is also seen in a plot of [C II]/FIR versus FIR (Fig. 7). The abrupt increase of the [C II]/FIR ratio occurs at about 4.5 kpc radial distance in the north and in the south of the major axis. At this distance the morphology of the whole galaxy changes, as seen in optical images (Sharma et al. 2011). The change occurs just beyond the location of the prominent spiral arms. It also occurs in a region where the H I/CO ratio rapidly increases (Fig. 4). As the O/H abundance gradient in M 33 is shallow with a slope of only ~−0.035 dex kpc^{-1} and with no signs of a break

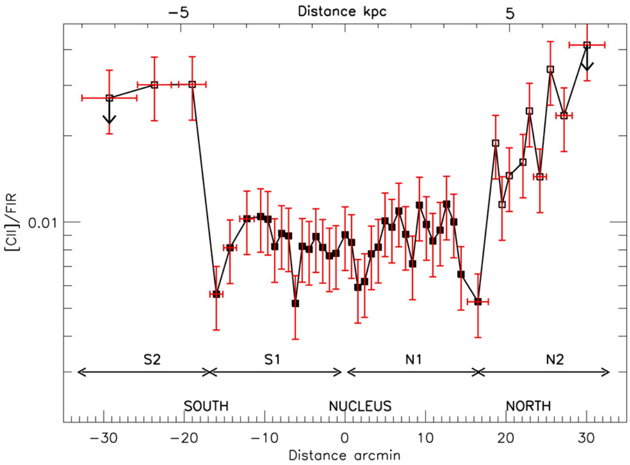

Fig. 6. Radial distribution of the [C II]/FIR ratio along the major axis of M 33.

(Magrini et al. 2010), the metallicity cannot be key for the sudden increase of the [C II]/FIR ratio.

Though only few studies of the radial variation of the [C II]/FIR ratio in galaxies exist, observations of M 31, M 51, NGC 6946, and the Milky Way indicate that this ratio rises with galacto-centric distance. Rodriguez-Fernandez et al. (2006) present a discussion of ISO/LWS maps of a portion of the northern arm of M 31 at 12 kpc distance from the nucleus. These data show a rather constant and high ratio of 2%. In contrast, the nucleus shows only 0.6%. M 31 is at the same distance as M 33; the LWS observations of M 31 sample the same linear scale as the present observations of M 33. In a later section, we attempt to interpret the radial variation found along the major axis of M 33 using PDR models.

In M 33, the [C II]/FIR ratio drops with increasing FIR luminosity, $L_{\rm FIR}$. A power law fit to the entire data set results in [C II]/FIR $\propto L_{\rm FIR}^{-0.34}$ (r = 0.83). A fit to the data of the outer disk only results in a slightly steeper slope (Fig. 7). In this figure, we also compare the M 33 data with those of other galaxies. Relative to the normal galaxies observed by Malhotra et al. (2001) the M 33 data are located in the region of low FIR luminosities $L_{\rm FIR} = 10^5{-}10^7\,L_\odot$ and high [C II]/FIR ratios of between 0.6% and 3%. The M 33 data lie in the same region as the data of the LMC, SMC and IC10.

The FIR luminosities of the low-metallicity systems are not directly comparable because their distances differ. However, the [C II] and FIR values of the LMC and SMC were taken from maps where the fluxes were averaged over individual sources from 35 to 70 pc in size, while the data were taken at a range of 14 to 16 pc linear resolutions (Israel et al. 1996; Israel & Maloney 2011). The IC 10 observations have a resolution of 290 pc (Madden et al. 1997), similar to that of the M 33 ISO/LWS data.

The M 33 data in Fig. 7 lie in the high limit of [C II]/FIR ratios which are found in the sample of normal galaxies using ISO/LWS (Malhotra et al. 2001). The latter appears on the right side of the plot of [C II]/FIR = 0.01%–0.7% and $L_{\rm FIR} = 10^7{-}10^{11}\,L_\odot$, which shows an average [C II]/FIR ratio of 0.32%. The [C II]/FIR ratios in M 33 are 25–200 times higher than in Milky Way star-forming regions for a similar $L_{\rm FIR}$ range, while this factor decreases an order of magnitude (2.5–20) in Galactic GMCs.

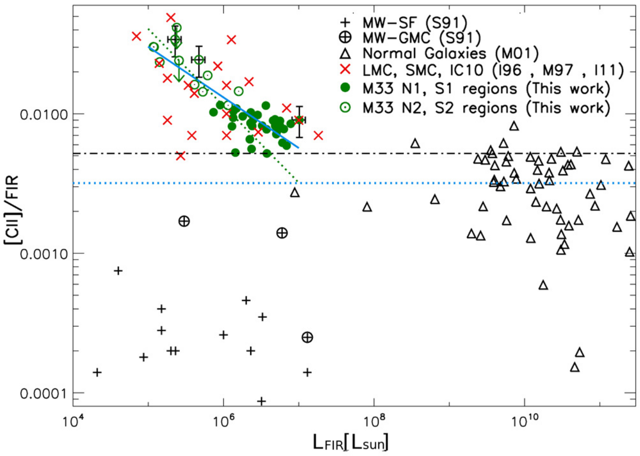

Fig. 7. [C II]/FIR ratio as function of $L_{\rm FIR}$. The blue solid line shows a linear fit to the whole data set of M 33 while the green dotted line shows a linear fit to N2 and S2 points of the outer galaxy only. The black dashed-dotted horizontal line shows the lower [C II]/FIR value found in our data set of M 33. The blue dotted horizontal line shows the average [C II]/FIR value in normal galaxies (Malhotra et al. 2001, M01). We also show data of Milky Way regions (Stacey et al. 1991, S91) and the low-metallicity objects LMC, SMC, IC 10 (Israel et al. 1996, I96), (Israel & Maloney 2011, I11), (Madden et al. 1997, M97).

3.4. M 33: A bridge between dwarf and normal galaxies?

After comparing the [C II]/FIR differences between M 33 and normal galaxies, we also compared CO/FIR and [C II]/CO ratios found in M 33 with those of other sources (Fig. 8). In these plots, we find four mostly disjunct groups of ratios. There is a group formed by both low-metallicity objects and ratios of the outer galaxy of M 33 (N2, S2). The M 33 ratios of the inner galaxy (N1, S1) form another group, which connects low-metallicity objects with normal galaxies, and Milky Way GMCs (S91), which form the third group. Finally, PDRs in the Milky Way that are exposed to high FUV fields (MW SF regions, S91) form the fourth group. For normal galaxies, the [C II]/CO 1–0 ratio increases with [C II]/FIR. For M 33 and other low-metallicity objects, the FIR/CO 1–0 ratios increase strongly with increasing [C II]/CO 1–0. This correlation is also seen for normal galaxies, though with increased scatter. The data points of the inner disk of M 33 lie between the data of the normal galaxies at low [C II]/CO ratios and the data of the other low-metallicity systems, which show high [C II]/CO ratios.

On average, the inner parts of M 33 (N1, S1) exhibit lower [C II]/CO and FIR/CO ratios than the other low-metallicity objects. This finding suggests that CO is less photo-dissociated in the inner disk of M 33 than in the outer regions (S2, N2) and than in the other low-metallicity objects. In the next paragraphs we will compare the observed ratios with the predictions of PDR models.

4. Discussion

4.1. Diagnostic diagram of [CII] /FIR vs. CO/FIR

In Fig. 9, we plot luminosities of [C II] versus CO, which are normalized with FIR luminosities. To this diagnostic diagram, we added observations of other galaxies, the corresponding lines of constant FUV-fields, and local volume densities of standard K99 PDR models which use a cloud optical extinction of $A_{\rm V}$ = 10 mag and solar metallicities. For completeness, we show

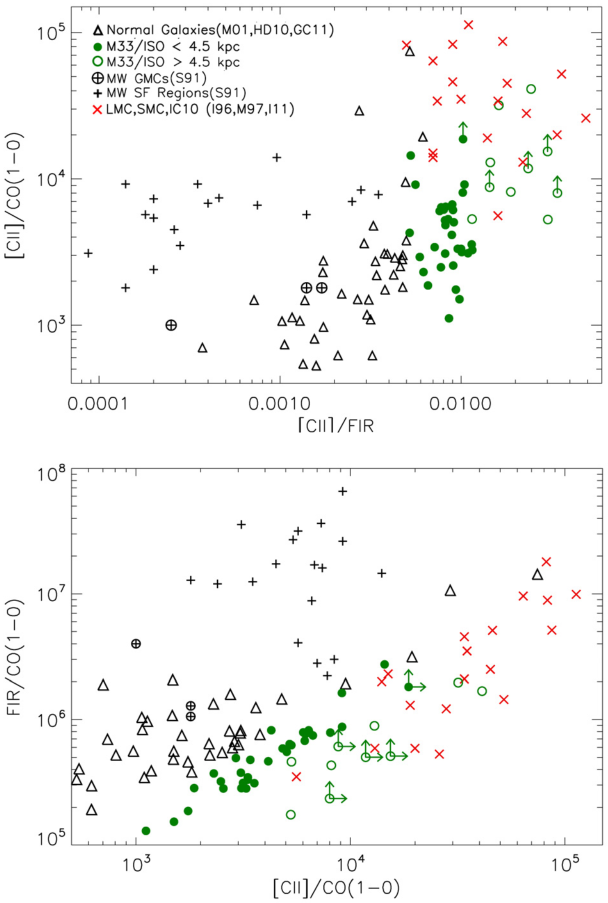

Fig. 8. Diagnostic plots of the ratios of [C II], CO and the FIR continuum for M 33 and for four other types of objects, low-metallicity systems, normal galaxies, Milky Way star-forming regions, and GMCs. *Upper panel*: [C II]/CO 1−0 vs. [C II]/FIR. *Bottom panel*: FIR/CO 1−0 vs. [C II]/CO 1−0. All panels are shown on a logarithmic scale. Symbols used have the same meaning than those used in Fig. 7.

Table 3. Range of densities and FUV fields consistent with the standard K99 PDR model for sources that are shown in the diagnostic plot of [C II]/FIR vs. CO/FIR (Fig. 9).

Objects	[C II]/(CO 1−0)	n [cm^{-3}]	G_0
M 33 (N1-S1)	1000−8000	$<10^4$	$<10^3$
M 33 (N2-S2)	5000−4.1 10^4	–	–
MW-SF	1000−5000	10^2−10^6	10^3−>10^4
MW-GMCs	500−1000	10^5−10^6	500−$\gtrsim 10^3$
Normal galaxies	500−4000	10^3−10^6	10^2−10^3
ULIRGs	500−4000	10^4−10^6	10^3−10^4
Starburst nuclei	~4100	10^3−10^4	500−$\gtrsim 10^3$
Non-starburst nuclei	500−4000	10^5−10^5	10^2−10^3
LMC, SMC, IC 10	8000−10^5	–	–

Notes. For the outer regions of M 33 and for the LMC, SMC, and IC 10, the standard model fails.

[C II] vs. CO normalized with the total-infrared (TIR) luminosities in Appendix D.

4.1.1. Observations

M 33. The [C II]/FIR ratios, which are observed on scales of 280 pc in M 33, stay rather constant at ~0.8% in the inner parts of M 33, and rise to 3% in the outer regions, as already presented in the previous sections. The [C II]/CO 1−0 ratios vary between 1000 and 41 200, while the CO 1−0/FIR ratios vary between 4×10^{-7} and 8×10^{-6}.

On scales of 50 pc (12″), the [C II]/FIR ratio varies between 0.01% and 3% over the 2′ × 2′ map of the BCLMP 302 H II region, as seen in Mookerjea et al. (2011, M11)[3]. The bulk of [C II]/FIR ratios lie in the range of ~0.7%−1%. The CO 1−0/FIR ratios lie between 4×10^{-7} and 8×10^{-6}. Interestingly, the PACS observations of the 2′ × 2′ BCLMP 302 region, which lies at a galacto-centric distance of 2.1 kpc, cover the same range of [C II]/FIR and CO 1−0/FIR ratios, which are found with ISO/LWS along the entire major axis of M 33 up to 8 kpc.

Other galaxies. The [C II]/CO ratios found in the inner parts of M 33 lie in the same range of values, which are1 found in the bulk of the normal galaxies and ULIRGs shown here. The outer regions of M 33 show higher values, similar to those found in other low-metallicity systems.

The ISO/LWS [C II]/FIR ratios of M 33 are higher than in normal galaxies, which only exhibit [C II]/FIR ratios of up to 0.4%. The low-metallicity galaxies LMC, SMC, and IC 10 show high [C II]/FIR ratios, which are comparable to those found in M 33, as already discussed above. Local ULIRGs show CO/FIR ratios of less than 10^{-6}, while normal galaxies show higher ratios of up to 5×10^{-6}. M 33 shows slightly higher peak ratios of up to 8×10^{-6}.

4.1.2. PDR model results

Observations consistent with the standard model. Most of the [C II]/FIR and CO/FIR ratios observed in the inner disk of M 33 lie in the parameter space of local densities and FUV fields spanned by the standard PDR of K99 (solar metallicity $Z = 1.0$, $A_V = 10$ mag, Fig. 9). These ratios indicate densities of less than $\sim 10^4$ cm^{-3} and FUV fields of less than $G_0 \sim 10^3$ in units of the local interstellar value. Some of the ratios observed in the inner galaxy and all ratios observed in the outer disk are, however, not consistent with this standard model, as discussed below.

In the literature, the observed CO intensities have sometimes been multiplied by a factor of two for the comparison with the predictions of the Kaufman PDR model. Hailey-Dunsheath et al. (2010) argue that CO 1−0 is optically thick, stemming only from the front-side of FUV illuminated clouds, while the FIR emission is in general optically thin, stemming from the front and the backside of clouds. We do not apply any factor; instead we use the observed values and argue that the optical depth of the galactic CO emission on scales of 280 pc will be reduced because of the velocity dispersion by turbulence and the large-scale gradients and that an ad-hoc factor of two does not seem appropriate.

In the framework of the standard PDR model, normal galaxies, especially the ULIRGs, tend to be consistent with higher densities that are up to a few times of 10^6 cm^{-3} than that are typically found in M 33. The latter are also consistent with higher FUV fields of up to $\sim 10^4$. Table 3 summarizes the range of values returned by the standard K99 PDR model for the whole data sample shown in Fig. 9. Normal galaxy and starburst nuclei points with extreme high [C II]/CO values were ignored here.

---

[3] To convert the TIR values used by M11 into FIR, we used the FIR/TIR ratios derived from the greybody fits (Sect. 2.2, Table B.1). Two ISO/LWS positions, N49 and N50, lie in the region mapped by M11. We took the average FIR/TIR value for the conversion.

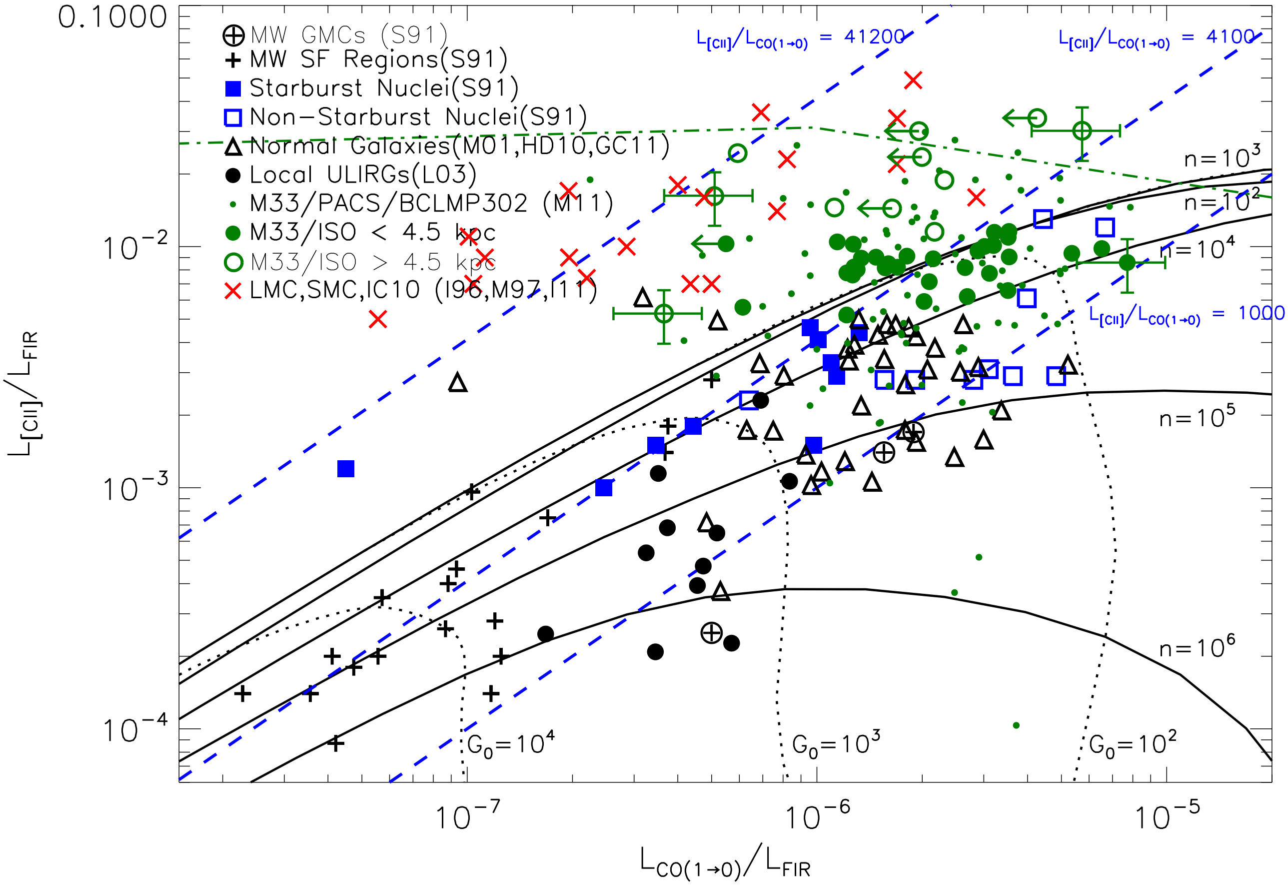

Fig. 9. [C II] versus CO, which are normalized with the FIR continuum. Big green filled circles show ISO/LWS data of the inner S1, N1 regions of M 33, while open circles show data of the outer S2, N2 regions. Small green circles show PACS observations of the BCLMP 302 H II region in M 33 (M11). In addition we show data from Milky Way GMCs, from star-forming regions, and from other galaxies, which are compiled from Stacey et al. (1991, S91), Hailey-Dunsheath et al. (2010, HD10), Graciá-Carpio et al. (2011, GC11), Israel et al. (1996, I96), Israel & Maloney (2011, I11), Madden et al. (1997, M97), Malhotra et al. (2001, M01), and Luhman et al. (2003, L03). The lowest [C II]/CO ratio observed with ISO/LWS in M 33 is 1000 (lower blue dashed line), while the highest ratio is 41 200 (upper blue dashed line). Black solid and dotted lines indicate lines of constant density n and FUV field G_0, respectively, from the standard K99 PDR model with $A_V = 10$ mag and solar metallicity $Z = 1$. The dashed-dotted green line shows a K99 PDR model result for $A_V = 1$ mag, $Z = 1$, and $n = 10^3\ \mathrm{cm}^{-3}$. The knee of this curve is for $G_0 = 10^{0.5}$ (cf. Fig. 18 in K99).

Observations inconsistent with the standard model. All ISO/LWS [C II]/FIR and CO/FIR ratios of the outer disk of M 33 are inconsistent with the standard PDR model for any density and FUV field. In general, [C II]/FIR ratios above 2% cannot be reproduced by the standard model for CO/FIR ratios which are less than 10^{-5}. For lower CO/FIR ratios, the upper limit of [C II]/FIR, which can be modeled, drops. For instance, the upper limit of [C II]/FIR lies near 0.5% at CO/FIR ∼ 10^{-6}.

The scatter of [C II]/FIR and CO/FIR data seen in M 33 on the large scales sampled by the ISO/LWS beam is similar to the scatter seen on small scales of 50 pc in the small subregion BCLMP 302. However, variations of metallicities are not expected on such small scales. The observed scatter of [C II]/FIR and CO/FIR ratio must therefore reflect the variation of other properties of the emitting gas and dust.

As shown in Figs. 9 and 10, K99 PDR models of low optical extinctions reproduce the high [C II]/FIR ratios observed predominantly in the outer disk of M 33. Assuming a total column density that corresponds to an A_V of only 1 mag and to solar metallicity, the ratios observed in the outer disk are consistent with $n \sim 10^3\ \mathrm{cm}^{-3}$ and $G_0 \sim 1$, while the ratios observed in the inner disk are consistent with somewhat higher densities and FUV fields of $n \sim 10^4\ \mathrm{cm}^{-3}$ and $G_0 \sim 10$ (Fig. 10). The ratio of G_0/n is about $10^{-3}\ \mathrm{cm}^3$ in both cases.

Subsolar metallicities are not needed to explain these data sets, because the curves for the models with subsolar metallicity $Z = 0.1$ are similar to the curves for $Z = 1.0$. This finding also shows that [C II] is relatively insensitive to changes in the metallicity. When [C II] dominates gascooling, the models indicate that the gas temperature of the PDR surface layer, which emits [C II] adjusts in a way that the emergent [C II] flux equals the FUV flux times the gas heating efficiency (Kaufman et al. 2006).

Because the observed metallicity gradient of M 33 is shallow (Magrini et al. 2010), we do not suspect that the average optical extinction of clouds changes abruptly from about 10 mag to about 1 mag between the inner and outer disk of M 33. We suggest, instead, that the overall low-metallicity environment of M 33 is composed of clouds that have generally low optical extinctions of one or a few magnitudes.

In this scenario, the rather abrupt increase of heating efficiency beyond about 4.5 kpc radial distance is caused by a drop of average local densities of the molecular gas and a decrease of FUV field strengths. This drop of the FUV along the major axis of M 33 is already indicated by the radially averaged extinction

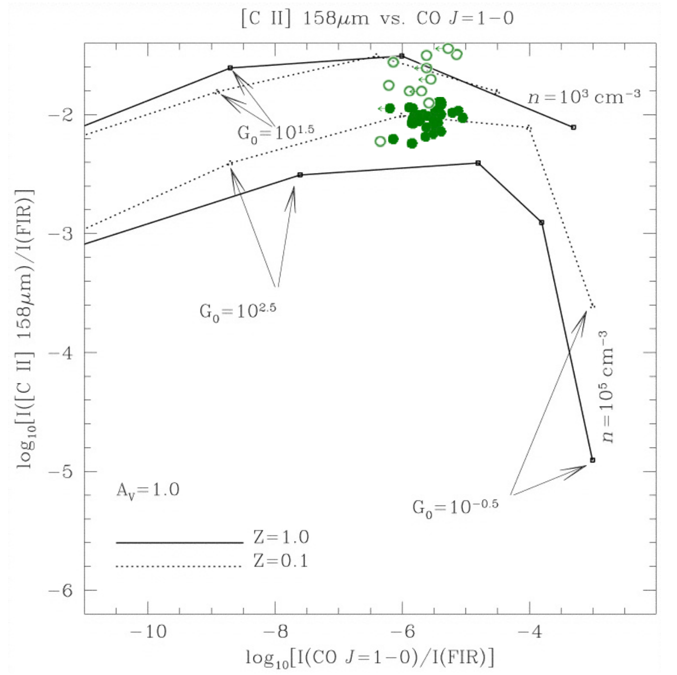

Fig. 10. [C II] versus CO, which are normalized with the FIR continuum (Fig. 18 of K99). Black solid and dotted lines indicate lines of constant density for metallicities of $Z = 1.0$ and $Z = 0.1$, respectivey, from the K99 PDR model using $A_V = 1$ mag. Big green filled circles show ISO/LWS data of the inner S1, N1 regions of M 33, while open circles show data of the outer S2, N2 regions.

corrected FUV fluxes (cf. Fig. 3 in Verley et al. 2009). Verley et al. (2007) did IR photometry of 515 compact sources. The best models to reproduce the extinction seen in these H II regions are the ones with $A_V < 10$ mag.

The change of density from 10^4 in the inner disk to 10^3 in the outer disk would imply that PDRs in the outer disk are typically about a factor of 10 larger in size than in the inner disk:

$$\frac{r_{\rm outer}}{r_{\rm inner}} = \frac{N({\rm H_2})_{\rm outer}/n({\rm H_2})_{\rm outer}}{N({\rm H_2})_{\rm inner}/n({\rm H_2})_{\rm inner}} \sim 10. \tag{1}$$

We estimated the FUV field in Habing units (Habing 1968) directly from the FIR continuum. We used $G_0 = 4\pi I_{\rm FIR}/1.6\times10^{-3}$ in erg $\rm s^{-1}\,cm^{-2}$ (Mookerjea et al. 2011; Kaufman et al. 1999) and obtained $G_0 = 28$ for the nucleus and $G_0 = 1.3$ for the N66 position in the outer disk of M 33. The low FUV field found in the outer disk is consistent with the radiation field predicted by the K99 PDR model from the [C II]/FIR and CO/FIR ratios for low extinctions.

For a fixed CO/FIR ratio, a given density, and a given metallicity, the modelled [C II]/FIR decreases with increasing optical extinction (Figs. 16–18 in Kaufman et al. 1999). For example, log([C II]/FIR) decreases by a factor ∼5 from −1.5 at 1 mag to −2.2 at 10 mag at log (CO/FIR) = 6, In clouds of low optical extinctions, FUV photons penetrate deeper into the cloud. For spherical clouds, the smaller CO core is surrounded by a larger [C II] emitting region, which leads to enhanced [C II]/CO ratios (cf. Bolatto et al. 1999; Röllig et al. 2006). The observed high [C II]/FIR and [C II]/CO ratios are best explained by clouds of low columns (optical extinctions) which lead to an increase of the [C II] layer relative to the total gas traced by CO. Such clouds also lead to an increase of the [C II] emission relative to the total dust traced by the FIR continuum. We propose that reduced volume densities and the geometrical dilution of the FUV field, when photons can enter more deeply, are of secondary importance only.

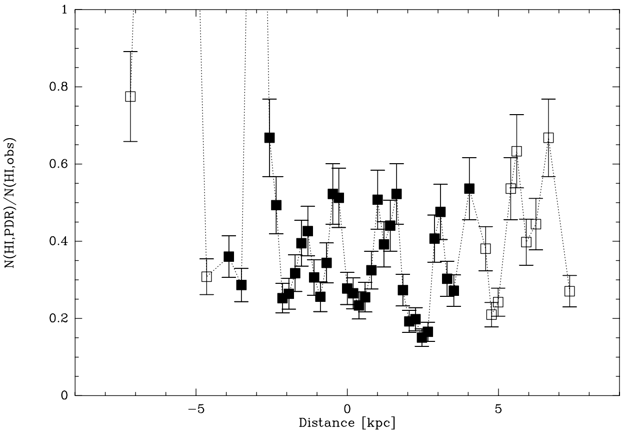

Fig. 11. Fraction of H I column density, which stem from PDRs. Errorbars only show the 15% observational error of H I intensities. Two positions in the south, where N(H I,PDR)> N(H I,obs), are not shown.

The low optical extinctions are consistent with a reduced dust-to-gas ratio in the low-metallicity environment of M 33. As discussed by Israel et al. (1996) and Israel & Maloney (2011) using data of the LMC, the ratio of total gas column density over optical extinction, $N_{\rm H}/A_V$, increases in low-metallicity environments.

4.2. HI emission from PDRs

In the following, we assume that all observed H I emission stems from the cold neutral and atomic medium (CNM) and from PDRs. Before discussing a possible contribution of [C II] emission from the CNM, we first need to study the H I fraction, which stem from PDRs. At the surface of PDRs, molecular hydrogen is photodissociated and a layer of atomic hydrogen is formed. The column from H I is a function of impinging FUV field over the volume density of the molecular gas, G_0/n, as shown e.g. by Sternberg (1988). Stacey et al. (1991) studied the contribution of H I emission from PDRs to the total hydrogen column in a sample of galaxies. With the typical densities and FUV fields derived above for M 33, we find a typical G_0/n ratio of 10^{-3} cm^3 in the inner and outer disk of M 33. Next, we use Eq. (3) of Heiner et al. (2011):

$$N({\rm HI,PDR}) = \frac{7.8\times10^{20}}{D}\,\ln\left(1+\frac{106\,G_0}{n}\,D^{-0.5}\right)\,{\rm cm^{-2}}, \tag{2}$$

where the dust-to-gas ratio D is normalized to the solar neighborhood value of (12 + log(O/H)) – 8.69 (Eq. (2) of Heiner et al. 2011) and a constant oxygen abundance of 12+log (O/H) = 8.27 (see references in Buchbender et al. 2013). This calculation leads to a constant H I column density, which stem from PDRs of 3.25×10^{20} cm^{-2}.

In Fig. 11, we compare the H I column density from PDRs to the observed beam-averaged H I column density, assuming that the PDRs fill the beam. We did not attempt detailed PDR modeling to derive the beamfilling factor (e.g. by comparing the observed FIR continuum with the best fitting FUV field from models). Stacey et al. (1991) derived a typical beamfilling factor of 0.3 for the sample of galaxies they studied. In M 33, the estimated fraction of H I column densities, which stem from PDRs stays between 15% and 70% for all data between 2 kpc radial distance in the south and 7.3 kpc in the north. Two positions further south exhibit very low H I columns, which are lower than the estimated H I column from PDRs; their N(H I,PDR)/N(H I,obs) ratios rise above 1 to values of up to 4, which indicates that the underlying assumptions of G_0, n, and the beam filling factor are not valid for these regions.

4.3. [CII] from the atomic medium

We investigate here which fraction of the observed [C II] emission could stem from the atomic cold neutral medium (CNM) in M 33. As described in Sect. 3.1, the emission of H I drops only weakly towards the outskirts, while the CO emission drops steeply (Fig. 2). In the southern part of the strip, the H I/CO rises continuously from a minimum in the center towards the outskirts at about a radial distance of 5 kpc (Fig. 4). On the other hand, the H I/CO in the north shows an abrupt increase at about a radial distance of 4.5 kpc, which is the same distance where the [C II]/FIR ratio rises to values of ~3% (Fig. 6). The relative contribution of the atomic gas that traces the CNM to the total gas emission (CO+H I) rises with galacto-centric distance. The H I/[C II] intensity ratio also rises strongly in the northern part of the strip over almost an order of magnitude (Fig. 5). This rise is because the [C II] emission drops more steeply with the radius than the H I. In the north, the observed [C II] emission has dropped by a factor of 27 relative to its value at the nucleus, while H I has dropped only by 40%. Any contribution of the CNM to the [C II] emission relative to the contribution from PDRs should be most prominent in the outskirts.

We note that the correlation between H I and [C II] emission is rather weak throughout the strip and also in the outskirts (cf. Fig. 3). Mookerjea et al. (2011) and Braine et al. (2012) studied [C II] HIFI spectra in two regions of $\sim 1'-2'$ along the major axis of M 33 at radial distances of 2.1 and 3.3 kpc. In both sources, the H I lines are systematically shifted relative to the [C II] lines by about 5 km s^{-1}. In addition, H I linewidths are about 30% broader than those of [C II]. These findings indicate that the [C II] emission, in at least these two regions of the inner galaxy, does not trace only the atomic medium.

To quantify a possible contribution of the cold neutral medium (CNM) to the [C II] emission, we use the H I line intensity, which is corrected for the contribution from PDRs, to derive the intensity of the [C II] line (cf. Crawford et al. 1985; Madden et al. 1993, 1997; Langer et al. 2010). Here, we assume optically thin emission of [C II] and H I, and beamfilling factors of unity. We estimate the [C II] intensities, which stem from the remaining fraction of the atomic gas via

$$\begin{aligned} I'(\mathrm{HI}) &= 3.35\times10^{14}\,I(\mathrm{HI}) && (3)\\ N(\mathrm{HI}) &= 1.82\times10^{18}\,I'(\mathrm{HI}) && (4)\\ N(\mathrm{HI,CNM}) &= N(\mathrm{HI})-N(\mathrm{HI,PDR}) && (5)\\ N(\mathrm{C}^+,\mathrm{CNM}) &= X_{\mathrm{C}^+}\,N(\mathrm{HI,CNM}) && (6)\\ I(\mathrm{C}^+,\mathrm{CNM}) &= 2.35\times10^{-21}N(\mathrm{C}^+) && (7)\\ &\times\left(\frac{2\,\exp(-\Delta E/T)}{1+2\,\exp(-\Delta E/T)+(n_{\mathrm{cr}}/n)}\right), && (8)\end{aligned}$$

where intensities I are in units of erg s^{-1} cm^{-2} sr^{-1}, I' in K km s^{-1}, and column densities in cm^{-2}. The energy of the [C II] $^2P_{3/2}$ state above ground is $\Delta E = h\nu/k = 91.3$ K, and the critical density for collisions with hydrogen atoms and/or molecules is $n_{\mathrm{cr}} = 3\times10^3$ cm^{-3} (cf. discussion and references in Langer et al. 2010). The fractional abundance $X(\mathrm{C}^+)$ of C$^+$ in the gas with respect to H I lies in the range of 1.4 to 1.8×10^{-4} in the local ISM of the Milky Way (Sofia et al. 1997). For the average low-metallicity environment of M 33, we assume $X(\mathrm{C}^+) = 0.6\times10^{-4}$ (Magrini et al. 2010; Henry et al. 2000). In addition, we assume diffuse atomic clouds of $n = 100$ cm^{-3} and $T = 80$ K, which corresponds to a pressure of about 8000 K cm^{-3} and is typical for the diffuse atomic medium in the Milky Way (e.g. Wolfire et al. 1995; Dickey et al. 2000). Higher temperatures and densities would increase the [C II] intensities but quickly become inconsistent with the generally accepted values for the pressure of the Galactic atomic ISM (cf. discussion in Sect. 4.2.1. of Madden et al. 1993).

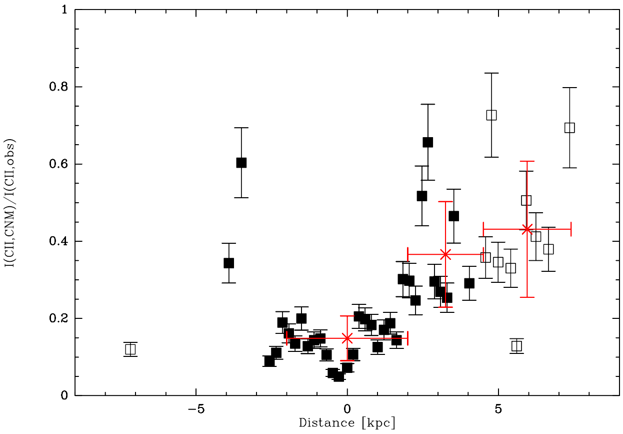

Fig. 12. Fraction of the observed [C II] emission stemming from the cold neutral medium for $T = 80$ K and $n = 100$ cm^{-3}, after correction of the observed H I for the contribution from PDRs. Squares mark the individual data along the major axis. Their errorbars only include the 15% observational error of the H I intensities. Crosses in red mark the fractions averaged over the inner 2 kpc, the northern 2 to 4.5 kpc, and the outer, northern disk between 4.5 and 7.4 kpc. Corresponding errorbars show the standard deviation of the individual data and the radius interval over which the values were binned.

Figure 12 shows the estimated fraction of the observed [C II] intensity, which stems from the CNM. As expected from the observed ratio of H I over [C II] intensities, the fraction is lowest in the nucleus and generally rises towards the outskirts. Towards the southern half, the CNM fraction shows strong variability, reflecting the variations of H I emission on small scales (cf. Fig. 2). However, the fraction rises towards the north generally from 20% ± 6% in the inner 2 kpc, to 37% ± 14% for radii between 2 and 4.5 kpc, to 43% ± 18% for radii between 4.5 and 7.4 kpc.

The rise of [C II]/FIR by a factor of more than three may therefore be partially explained by a rising contribution of the CNM to the [C II] emission, while the [C II]/FIR ratio of PDRs rises only moderately with only somewhat lowered values of A_V, n, and G_0 relative to the PDR models for the inner galaxy of $A_V\sim10$ mag, $n\sim10^4$ cm^{-3}, and $G_0\sim10$. A better knowledge of the temperature and density of the CNM is needed to derive more quantitative conclusions. We conclude that PDRs dominate in the inner parts of M 33, while both the CNM and PDRs can explain the [C II] emission observed in the outskirts.

4.4. The importance of the OI 63 μm line

A more complete study of the major gas cooling lines of the ISM would need to include the [O I] 63μm line as a tracer of high densities in PDRs. Higdon et al. (2003) detected this line at scales of 280 pc in the nucleus and toward five H II regions in M 33, where they found [C II]/[O I] ratios between 1.6 and 2.2.

Toward the H II region BCLMP 302 and on scales of 50 pc, the ratio varies betwen 2.5 and 10 (Mookerjea et al. 2011). Further *Herschel*/PACS and HIFI observations of several regions along the major axis of M 33 have been conducted in the framework of the `HerM33es` project to obtain a more complete dataset, which will allow more accurate estimates of the photoelectric heating efficiency, its variation on small scales, and the determination of gas properties (A_V, n, T) using PDR models.

5. Summary and conclusions

In this paper, we have studied ISO/LWS [C II] emission along the major axis of M 33 at scales of 280 pc. Stacking of few adjacent positions allowed detection of [C II] between galacto-centric distances of ~6 kpc in the south to ~6.7 kpc in the north. The radial distributions of the [C II]/CO and H I/CO ratios show an increase from the inner regions to the outer regions. While the H I/CO ratio has a minimum near the nucleus, the [C II]/CO ratio shows a minimum at about 10′ to the north, which corresponds to the global maximum of CO emission along the major axis.

The radial distribution of [C II] shows a strong correlation with star-formation tracers, the FIR continuum, and Hα emission, which closely follows the spiral arm structure. The correlation becomes weaker in the outskirts of M 33 beyond a galactocentric distance of 4.5 kpc.

The [C II]/FIR ratio remains constant at ~0.8% in the central 4.5 kpc radius and then increases rapidly to values of up to 3%. The [C II]/FIR ratio is a strong function of the FIR luminosity. The highest [C II]/FIR ratios are found for the lowest FIR luminosities. Other low-metallicity systems (LMC, SMC, IC 10) show similar [C II]/FIR ratios to M 33, which are higher than those found in the Milky Way and in normal galaxies.

The variation of [C II]/FIR and CO/FIR ratios found in a small 2′ × 2′ H II region of M 33 on small scales of 50 pc (Mookerjea et al. 2011) is very similar to the variation found with the ISO/LWS observations. This similarity is another indication that metallicity variations play a minor role in determining the [C II]/FIR ratio.

Diagnostic plots of [C II]/FIR vs. CO/FIR or FIR/CO vs. [C II]/CO show smooth transitions from normal galaxies to the positions in the inner 4.5 kpc radius of M 33 and to the outer parts of M 33 together with the other low-metallicity systems. Observations of the inner disk of M 33 serve as a bridge between normal galaxies exhibiting low [C II]/FIR and low [C II]/CO ratios to the low-metallicity systems, which show high [C II]/FIR and high [C II]/CO ratios.

The relative lack of dust shielding in the low-metallicity systems enhances CO photo-dissociation, hence, increases the [C II]/CO ratios. The standard K99 PDR models of 10 mag optical extinction fail to reproduce the high end of the observed [C II]/FIR and [C II]/CO ratios. However, models of low optical extinction expected in the low-metallicity environment of M 33 do reproduce the observed ratios for a constant metallicity. In the framework of models where $A_V = 1$ mag, the variation of observed [C II]/FIR ratios is caused by variations of the local densities that drop from about 10^4 cm^{-3} in the inner disk to 10^3 cm^{-3} in the outer parts. In addition, FUV field strengths reach to about 10 times the average interstellar radiation field in the inner disk, while dropping to only a few in the outskirts. High FUV fields tend to lower the photoelectric heating efficiency as grains and PAHs become positively charged (Okada et al. 2013). In contrast, the high [C II]/FIR ratios observed in low-metallicity galaxies can be caused by geometric dilution of low FUV fields in clouds of normal densities where carbon stays ionized.

In addition to PDRs, the atomic CNM traced by H I may contribute to the observed [C II] emission. Therefore, the above scenario may need to be revised. We conclude that the CNM, which is corrected for the H I emission from PDRs, contributes ~15% to the [C II] observed in the inner radius of 2 kpc. However, the CNM may contribute about 40% of the observed [C II] in the outer, northern disk, where H I emission is much stronger relative to [C II].

Acknowledgements. We thank S. Hailey-Dunsheath and J. Gracia-Carpio for providing us data shown in Fig. 9. We thank an anonymous referee for insightful comments.

References

Bakes, E. L. O., & Tielens, A. G. G. M. 1994, ApJ, 427, 822
Bolatto, A. D., Jackson, J. M., & Ingalls, J. G. 1999, ApJ, 513, 275
Boquien, M., Calzetti, D., Combes, F., et al. 2011, AJ, 142, 111
Braine, J., Gratier, P., Kramer, C., et al. 2012, A&A, 544, A55
Brauher, J. R., Dale, D. A., & Helou, G. 2008, ApJS, 178, 280
Buchbender, C., Kramer, C., Gonzalez-Garcia, M., et al. 2013, A&A, 549, A17
Cox, P., Krips, M., Neri, R., et al. 2011, ApJ, 740, 63
Crawford, M. K., Genzel, R., Townes, C. H., & Watson, D. M. 1985, ApJ, 291, 755
Dale, D. A., & Helou, G. 2002, ApJ, 576, 159
Dickey, J. M., Mebold, U., Stanimirovic, S., & Staveley-Smith, L. 2000, ApJ, 536, 756
Engargiola, G., Plambeck, R. L., Rosolowsky, E., & Blitz, L. 2003, ApJS, 149, 343
Freedman, W. L., Wilson, C. D., & Madore, B. F. 1991, ApJ, 372, 455
Gardan, E., Braine, J., Schuster, K. F., Brouillet, N., & Sievers, A. 2007, A&A, 473, 91
Graciá-Carpio, J., Sturm, E., Hailey-Dunsheath, S., et al. 2011, ApJ, 728, L7
Gratier, P., Braine, J., Rodriguez-Fernandez, N. J., et al. 2010, A&A, 522, A3
Gratier, P., Braine, J., Rodriguez-Fernandez, N. J., et al. 2012, A&A, 542, A108
Gry, C., Swinyard, B., Harwood, A., et al. 2003, The ISO Handbook, Volume III – LWS – The Long Wavelength Spectrometer, eds. M. F. Kessler, et al.
Habart, E., Verstraete, L., Boulanger, F., et al. 2001, A&A, 373, 702
Habing, H. J. 1968, Bull. Astron. Inst. Netherlands, 19, 421
Hailey-Dunsheath, S., Nikola, T., Stacey, G. J., et al. 2010, ApJ, 714, L162
Heiner, J. S., Allen, R. J., & van der Kruit, P. C. 2011, MNRAS, 416, 2
Henry, R. B. C., Edmunds, M. G., & Köppen, J. 2000, ApJ, 541, 660
Higdon, S. J. U., Higdon, J. L., van der Hulst, J. M., & Stacey, G. J. 2003, ApJ, 592, 161
Hollenbach, D. J., & Tielens, A. G. G. M. 1997, ARA&A, 35, 179
Hoopes, C. G., & Walterbos, R. A. M. 2000, ApJ, 541, 597
Hunter, I., Dufton, P. L., Smartt, S. J., et al. 2007, A&A, 466, 277
Israel, F. P., & Maloney, P. R. 2011, A&A, 531, A19
Israel, F. P., Maloney, P. R., Geis, N., et al. 1996, ApJ, 465, 738
Jakob, H., Kramer, C., Simon, R., et al. 2007, A&A, 461, 999
Kaufman, M. J., Wolfire, M. G., Hollenbach, D. J., & Luhman, M. L. 1999, ApJ, 527, 795
Kaufman, M. J., Wolfire, M. G., & Hollenbach, D. J. 2006, ApJ, 644, 283
Kessler, M. F., Steinz, J. A., Anderegg, M. E., et al. 1996, A&A, 315, L27
Kramer, C., Buchbender, C., Xilouris, E. M., et al. 2010, A&A, 518, L67
Langer, W. D., Velusamy, T., Pineda, J. L., et al. 2010, A&A, 521, L17
Luhman, M. L., Satyapal, S., Fischer, J., et al. 2003, ApJ, 594, 758
Madden, S. C., Geis, N., Genzel, R., et al. 1993, ApJ, 407, 579
Madden, S. C., Poglitsch, A., Geis, N., Stacey, G. J., & Townes, C. H. 1997, ApJ, 483, 200
Magrini, L., Stanghellini, L., Corbelli, E., Galli, D., & Villaver, E. 2010, A&A, 512, A63
Malhotra, S., Kaufman, M. J., Hollenbach, D., et al. 2001, ApJ, 561, 766
Mizutani, M., Onaka, T., & Shibai, H. 2004, A&A, 423, 579
Mookerjea, B., Kramer, C., Buchbender, C., et al. 2011, A&A, 532, A152
Okada, Y., Pilleri, P., Berné, O., et al. 2013, A&A, 553, A2
Putman, M. E., Peek, J. E. G., Muratov, A., et al. 2009, ApJ, 703, 1486
Rodriguez-Fernandez, N. J., Braine, J., Brouillet, N., & Combes, F. 2006, A&A, 453, 77

Röllig, M., Ossenkopf, V., Jeyakumar, S., Stutzki, J., & Sternberg, A. 2006, A&A, 451, 917
Rubin, D., Hony, S., Madden, S. C., et al. 2009, A&A, 494, 647
Sharma, S., Corbelli, E., Giovanardi, C., Hunt, L. K., & Palla, F. 2011, A&A, 534, A96
Sofia, U. J., Cardelli, J. A., Guerin, K. P., & Meyer, D. M. 1997, ApJ, 482, L105
Stacey, G. J., Geis, N., Genzel, R., et al. 1991, ApJ, 373, 423
Stacey, G. J., Hailey-Dunsheath, S., Ferkinhoff, C., et al. 2010, ApJ, 724, 957
Sternberg, A. 1988, ApJ, 332, 400
Sturm, E., Bauer, O. H., Brauer, J., et al. 1998, in Astronomical Data Analysis Software and Systems VII, eds. R. Albrecht, R. N. Hook, & H. A. Bushouse, ASP Conf. Ser., 145, 161
Swinyard, B. M., Burgdorf, M. J., Clegg, P. E., et al. 1998, in SPIE Conf. Ser. 3354, ed. A. M. Fowler, 888
Tabatabaei, F. S., Beck, R., Krause, M., et al. 2007, A&A, 466, 509
Tielens, A. G. G. M., & Hollenbach, D. 1985, ApJ, 291, 722
Vastel, C., Spaans, M., Ceccarelli, C., Tielens, A. G. G. M., & Caux, E. 2001, A&A, 376, 1064
Verley, S., Hunt, L. K., Corbelli, E., & Giovanardi, C. 2007, A&A, 476, 1161
Verley, S., Corbelli, E., Giovanardi, C., & Hunt, L. K. 2009, A&A, 493, 453
Weingartner, J. C., & Draine, B. T. 2001, ApJS, 134, 263
Wolfire, M. G., Hollenbach, D., McKee, C. F., Tielens, A. G. G. M., & Bakes, E. L. O. 1995, ApJ, 443, 152
Xilouris, E. M., Tabatabaei, F. S., Boquien, M., et al. 2012, A&A, 543, A74

Pages 12 to 17 are available in the electronic edition of the journal at `http://www.aanda.org`

Appendix A: List of positions

Tables A.1 and A.2 list the 77 positions observed using ISO/LWS, their respective galacto-centric distance, and the detection of [C II].

Appendix B: Intensities at the observed ISO/LWS positions

The IRAM 30 m CO 2−1 data on the T_A^* scale were converted into $T_{\rm mb}$ temperatures using the forward efficiency $F_{\rm eff} = 0.90$ and the main beam efficiency $B_{\rm eff} = 0.49$: $T_{\rm mb} = (F_{\rm eff}/B_{\rm eff})\ T_A^*$. The CO 2−1 map was first smoothed from the original 11″ resolution to 22″ using a Gaussian kernel. To derive CO 1−0 intensities from the CO 2−1 data, we used a linear function of the 2−1/CO 1−0 ratio, which drops from 0.8 in the nucleus of M 33 to 0.5 at a galactocentric distance of 8.5 kpc (Gratier et al. 2010). Next, we smoothed the map to the ISO/LWS resolution and converted the data to intensities in erg $\rm cm^{-2}\ s^{-1}\ sr^{-1}$.

Both the H I data and the Hα data were also smoothed to the LWS resolution. The original resolutions of the H I data were 11″, while we assumed an original pencil beam for the Hα data. Table B.1 lists the resulting integrated intensities of [C II], H I, Hα, CO 2−1, 1−0, the FIR continuum, and the TIR/FIR ratio for all positions and stacked areas.

Appendix C: Sample [CII] ISO/LWS spectra and SEDs

We show here four examples of the [C II] spectra and SEDs obtained. Figure 1a shows the only spectrum with a baseline fit of order one. Figure 1c shows the spectrum from the nucleus, where the lowest rms and highest flux are reached. The highest rms and the lowest flux peak of the four spectra are shown in position N61 (Fig. 1g), which belongs to the northern, outer N2 region. The SEDs show the strongest warm dust component in the nucleus (Fig. 1d), while the weakest warm component is seen in N61 (Fig. 1h). Cold dust components are similar in the inter-arm region (Fig. 1b), the nucleus, and in BCLM302 (Fig. 1f). The outer points also show weaker cold dust emission than the other regions.

Appendix D: [CII]/TIR vs. CO/TIR

For completeness, we show the diagnostic plot of [C II] vs. CO luminosities in Fig. D.1, which are normalized with the TIR luminosities derived from the two-greybody fits described in Sect. 2.2.

Table A.1. ISO/LWS positions observed in [C II] along the southern part of the major axis of M 33.

Pos ID (1)	RA (2)	Dec (3)	Ang. Dis [′] (4)	Lin. Dis [kpc] (5)	[C II] detection? (6)
S1	01:32:57	+30:10:06	−32.70	−7.99	S1-S8
S2	01:32:58	+30:10:52	−31.80	−7.77	S1-S8
S3	01:32:59	+30:11:38	−31.00	−7.57	S1-S8
S4	01:33:01	+30:12:24	−30.10	−7.35	S1-S8
S5	01:33:02	+30:13:10	−29.30	−7.16	S1-S8
S6	01:33:03	+30:13:56	−28.40	−6.94	S1-S8
S7	01:33:05	+30:14:42	−27.50	−6.72	S1-S8
S8	01:33:06	+30:15:28	−26.70	−6.52	S1-S8
S9	01:33:07	+30:16:14	−25.80	−6.30	S9-S14
S10	01:33:08	+30:17:00	−25.00	−6.11	S9-S14
S11	01:33:10	+30:17:46	−24.10	−5.89	S9-S14
S12	01:33:11	+30:18:32	−23.30	−5.69	S9-S14
S13	01:33:12	+30:19:18	−22.40	−5.47	S9-S14
S14	01:33:14	+30:20:04	−21.60	−5.28	S9-S14
S15	01:33:15	+30:20:50	−20.70	−5.06	S15-S19
S16	01:33:16	+30:21:36	−19.90	−4.86	S15-S19
S17	01:33:18	+30:22:22	−19.00	−4.64	S15-S19
S18	01:33:19	+30:23:08	−18.10	−4.42	S15-S19
S19	01:33:20	+30:23:54	−17.30	−4.23	S15-S19
S20	01:33:24	+30:24:40	−16.40	−4.01	S20-S21
S21	01:33:25	+30:25:27	−15.60	−3.81	S20-S21
S22	01:33:27	+30:26:13	−14.70	−3.59	S22-S23
S23	01:33:28	+30:26:59	−13.90	−3.40	S22-S23
S24	01:33:30	+30:27:45	−13.00	−3.18	S24-S26
S25	01:33:31	+30:28:31	−12.20	−2.98	S24-S26
S26	01:33:33	+30:29:17	−11.30	−2.76	S24-S26
S27	01:33:34	+30:30:03	−10.50	−2.57	X
S28	01:33:36	+30:30:49	−9.60	−2.35	X
S29	01:33:37	+30:31:35	−8.75	−2.14	X
S30	01:33:39	+30:32:21	−7.89	−1.93	X
S31	01:33:40	+30:33:07	−7.04	−1.72	X
S32	01:33:42	+30:33:53	−6.19	−1.51	X
S33	01:33:43	+30:34:39	−5.33	−1.30	X
S34	01:33:45	+30:35:25	−4.48	−1.09	X
S35	01:33:46	+30:36:11	−3.63	−0.89	X
S36	01:33:48	+30:36:57	−2.79	−0.68	X
S37	01:33:49	+30:37:43	−1.95	−0.48	X
S38	01:33:51	+30:38:29	−1.14	−0.28	X

Notes. Columns (4) and (5) list galacto-centric distances. Negative values indicate southern positions. Column (6) indicates whether [C II] emission was detected above 3σ at a given position (marked by "X") or were averaged over a given range of positions.

Table A.2. ISO/LWS positions observed in [C II] along the northern part of the major axis of M 33.

Pos ID (1)	RA (J2000) (2)	Dec (J2000) (3)	Ang. Dis [′] (4)	Lin. Dis [kpc] (5)	[C II] Detection? (6)
39 (Nucleus)	01:33:51	+30:39:37	0.00	0.00	X
N40	01:33:54	+30:40:01	.80	0.20	X
N41	01:33:55	+30:40:47	1.58	0.39	X
N42	01:33:57	+30:41:33	2.42	0.59	X
N43	01:33:58	+30:42:19	3.26	0.80	X
N44	01:34:00	+30:43:05	4.11	1.00	X
N45	01:34:01	+30:43:51	4.96	1.21	X
N46	01:34:03	+30:44:37	5.81	1.42	X
N47	01:34:04	+30:45:23	6.67	1.63	X
N48	01:34:06	+30:46:09	7.52	1.84	X
N49	01:34:07	+30:46:55	8.38	2.05	X
N50	01:34:09	+30:47:41	9.23	2.26	X
N51	01:34:10	+30:48:27	10.1	2.47	X
N52	01:34:12	+30:49:13	10.9	2.66	X
N53	01:34:13	+30:49:59	11.8	2.88	X
N54	01:34:15	+30:50:45	12.6	3.08	X
N55	01:34:16	+30:51:31	13.5	3.30	X
N56	01:34:18	+30:52:17	14.4	3.52	X
N57	01:34:19	+30:53:03	15.2	3.71	N57-N60
N58	01:34:21	+30:53:49	16.1	3.93	N57-N60
N59	01:34:23	+30:54:35	16.9	4.13	N57-N60
N60	01:34:24	+30:55:21	17.8	4.35	N57-N60
N61	01:34:26	+30:56:07	18.7	4.57	X
N62	01:34:27	+30:56:53	19.5	4.76	X
N63	01:34:29	+30:57:39	20.4	4.98	X
N64	01:34:30	+30:58:25	21.2	5.18	–
N65	01:34:32	+30:59:11	22.1	5.40	X
N66	01:34:33	+30:59:57	22.9	5.60	X
N67	01:34:35	+31:00:43	23.8	5.82	N67-N68
N68	01:34:36	+31:01:29	24.6	6.01	N67-N68
N69	01:34:38	+31:02:15	25.5	6.23	X
N70	01:34:39	+31:03:01	26.4	6.45	N70-N72
N71	01:34:41	+31:03:47	27.2	6.65	N70-N72
N72	01:34:42	+31:04:33	28.1	6.87	N70-N72
N73	01:34:44	+31:05:19	28.9	7.06	N73-N77
N74	01:34:45	+31:06:05	29.8	7.28	N73-N77
N75	01:34:47	+31:06:51	30.6	7.48	N73-N77
N76	01:34:48	+31:07:38	31.5	7.70	N73-N77
N77	01:34:50	+31:08:24	32.3	7.89	N73-N77

Notes. Columns (4) and (5) list galacto-centric distances. Column (6) indicates whether [C II] emission was detected above 3σ at a given position (marked by "X"), where the emission was averaged over a given range of positions, or whether no emission was detected (marked by "–").

Table B.1. Integrated intensities at the positions with [C II] detections.

Pos. ID	[C II]	H I	Hα	CO(2-1)	CO 1–0	FIR	TIR/FIR
S1-S8	**2.20e-06**	6.88e-13	**3.05e-07**	–	–	9.12e-05	2.52e+00
S9-S14	1.28e-06	1.37e-13	**3.11e-07**	**1.18e-09**	**8.32e-11**	4.25e-05	2.50e+00
S15-S19	1.26e-06	1.73e-12	8.68e-07	3.13e-09	2.39e-10	4.17e-05	2.47e+00
S20-S21	4.70e-06	1.48e-12	3.75e-06	6.35e-09	5.15e-10	8.39e-04	1.54e+00
S22-S23	3.75e-06	1.86e-12	1.20e-06	7.06e-09	5.87e-10	4.61e-04	1.89e+00
S24-S26	2.69e-06	2.00e-13	9.64e-07	**1.70e-09**	**1.44e-10**	2.62e-04	2.32e+00
S27	5.04e-06	7.98e-13	3.63e-06	3.10e-09	5.51e-10	4.82e-04	1.44e+00
S28	8.38e-06	1.08e-12	7.35e-06	5.92e-09	1.04e-09	8.19e-04	1.48e+00
S29	1.42e-05	2.11e-12	1.34e-05	1.69e-08	2.94e-09	1.73e-03	1.49e+00
S30	1.57e-05	2.02e-12	1.61e-05	1.81e-08	3.11e-09	1.72e-03	1.73e+00
S31	1.45e-05	1.68e-12	1.24e-05	1.28e-08	2.17e-09	1.62e-03	1.56e+00
S32	6.97e-06	1.35e-12	7.45e-06	9.68e-09	1.63e-09	1.34e-03	1.38e+00
S33	9.54e-06	1.25e-12	5.81e-06	8.88e-09	1.48e-09	1.16e-03	1.44e+00
S34	1.43e-05	1.74e-12	9.92e-06	1.41e-08	2.32e-09	1.78e-03	1.42e+00
S35	1.78e-05	2.08e-12	1.66e-05	2.75e-08	4.30e-09	2.00e-03	1.32e+00
S36	1.64e-05	1.55e-12	1.41e-05	2.02e-08	3.15e-09	2.01e-03	1.39e+00
S37	1.41e-05	1.02e-12	1.38e-05	1.50e-08	2.34e-09	1.85e-03	1.37e+00
S38	1.75e-05	1.04e-12	1.90e-05	1.75e-08	2.74e-09	2.25e-03	1.34e+00
39 (Nucleus)	3.27e-05	1.92e-12	2.77e-05	3.41e-08	5.34e-09	3.62e-03	1.34e+00
N40	2.36e-05	2.01e-12	1.52e-05	2.85e-08	4.45e-09	2.78e-03	1.33e+00
N41	1.45e-05	2.28e-12	1.03e-05	3.17e-08	4.96e-09	2.45e-03	1.39e+00
N42	1.34e-05	2.09e-12	8.94e-06	3.72e-08	5.81e-09	2.16e-03	1.40e+00
N43	1.03e-05	1.64e-12	9.89e-06	2.65e-08	4.14e-09	1.33e-03	1.69e+00
N44	7.00e-06	1.05e-12	4.74e-06	1.38e-08	2.27e-09	8.56e-04	1.47e+00
N45	8.27e-06	1.36e-12	5.99e-06	1.58e-08	2.62e-09	8.19e-04	1.73e+00
N46	6.15e-06	1.21e-12	4.08e-06	1.11e-08	1.85e-09	6.41e-04	1.68e+00
N47	5.77e-06	1.02e-12	2.85e-06	1.10e-08	1.86e-09	5.28e-04	1.63e+00
N48	8.00e-06	1.95e-12	4.71e-06	1.83e-08	3.13e-09	8.83e-04	1.48e+00
N49	1.28e-05	2.77e-12	1.56e-05	2.17e-08	3.75e-09	1.79e-03	1.43e+00
N50	1.49e-05	2.69e-12	1.41e-05	2.39e-08	4.18e-09	1.30e-03	1.89e+00
N51	9.91e-06	3.54e-12	5.56e-06	3.73e-08	6.59e-09	1.01e-03	1.96e+00
N52	6.98e-06	3.22e-12	2.96e-06	3.51e-08	6.27e-09	8.13e-04	1.83e+00
N53	4.48e-06	1.31e-12	1.37e-06	1.41e-08	2.56e-09	4.78e-04	1.42e+00
N54	3.72e-06	1.12e-12	2.21e-06	6.24e-09	1.14e-09	3.22e-04	1.78e+00
N55	8.24e-06	1.76e-12	1.43e-05	1.34e-08	2.48e-09	8.23e-04	1.72e+00
N56	5.23e-06	1.96e-12	1.26e-05	1.50e-08	2.80e-09	7.96e-04	1.69e+00
N57-N60	2.70e-06	9.94e-13	2.69e-06	2.27e-09	1.87e-10	5.12e-04	1.56e+00
N61	4.13e-06	1.40e-12	2.26e-06	2.55e-09	5.07e-10	2.19e-04	1.90e+00
N62	4.71e-06	2.54e-12	5.81e-06	4.41e-09	8.87e-10	4.09e-04	1.74e+00
N63	8.22e-06	2.20e-12	8.17e-06	3.11e-09	6.35e-10	5.66e-04	1.46e+00
N65	2.38e-06	9.94e-13	1.26e-06	3.57e-10	7.48e-11	1.47e-04	1.75e+00
N66	4.10e-06	8.42e-13	8.15e-06	3.86e-10	9.97e-11	1.68e-04	1.71e+00
N67-N68	2.72e-06	1.34e-12	4.44e-06	**4.26e-10**	**3.10e-10**	1.89e-04	2.70e+00
N69	2.76e-06	1.20e-12	1.31e-06	**4.89e-09**	**3.45e-10**	8.09e-05	2.08e+00
N70-N72	1.19e-06	7.98e-13	**3.19e-07**	**1.45e-09**	**1.01e-10**	5.06e-05	2.12e+00
N73-N77	**3.53e-06**	1.97e-12	**5.25e-07**	**4.24e-10**	**2.83e-11**	8.51e-04	2.31e+00

Notes. Intensities are given in erg s^{-1} sr^{-1} cm^{-2} at the angular resolution of the [C II] data. Values in bold face are upper limits.

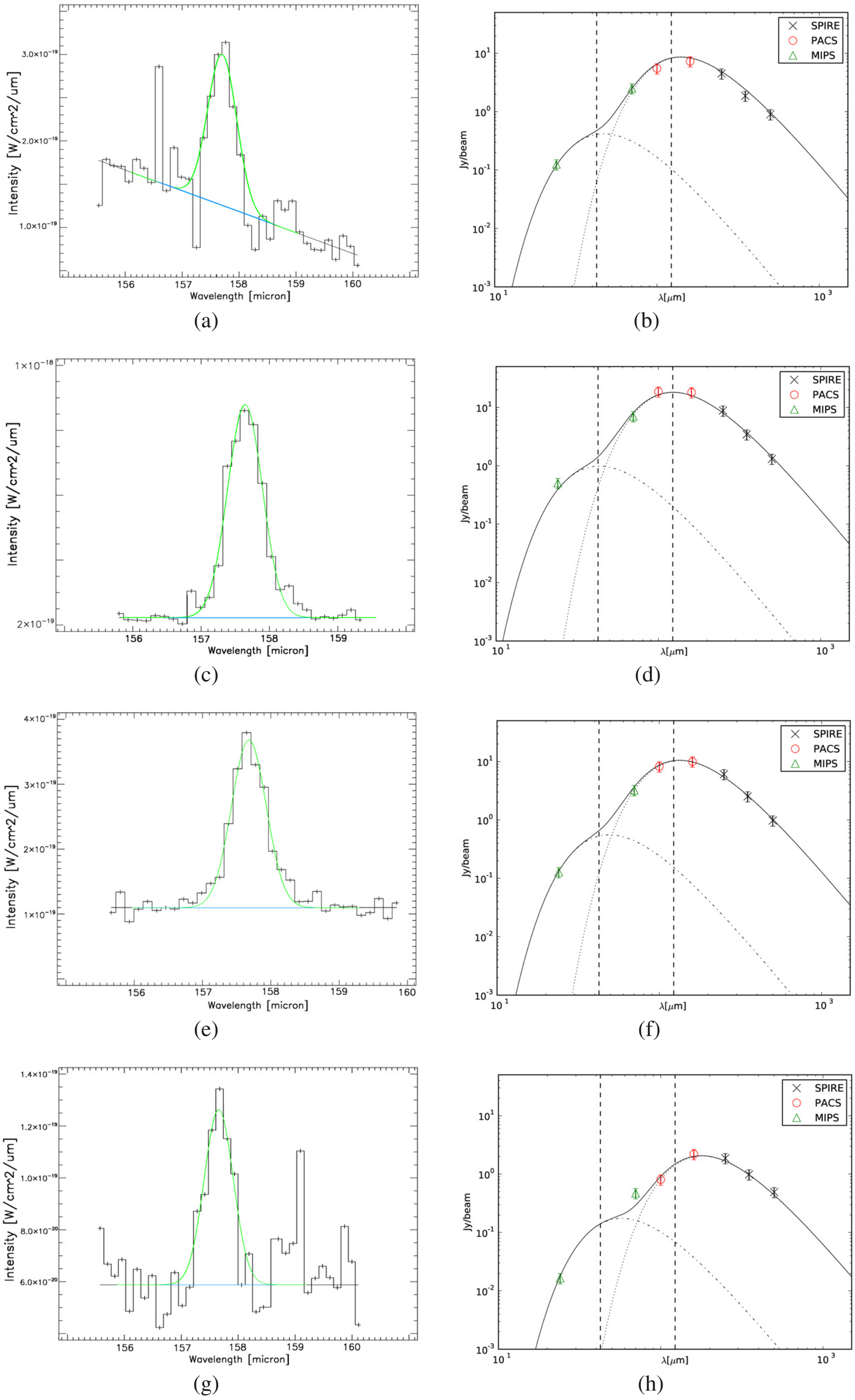

(a) (b)

(c) (d)

(e) (f)

(g) (h)

Fig. C.1. Examples of some of the [C II] ISO/LWS spectra and SEDs obtained in this work. The vertical dashed lines mark the integration interval to derive the FIR continuum, 42.5 μm and 122.5μm (Dale & Helou 2002). **a)**, **b)** The first row shows the [C II] spectrum and the SED of the inter-arm position S32. **c**, **d)** The second row shows the spectrum and SED from the nucleus of M 33. **e)**, **f)** The third row shows observations of the H II region BCLMP 302 (N49). **g)**, **h)** Finally, the last row shows the spectrum and the SED from one of the positions (N61) in the outer, southern N2 region. The SEDs show MIPS 24 μm and 70 μm, PACS 100 μm and 160 μm and SPIRE 250 μm, 350 μm and 500 μm data. In the [C II] spectra, green lines show Gaussian fits to the spectra and blue lines show fitted baselines.

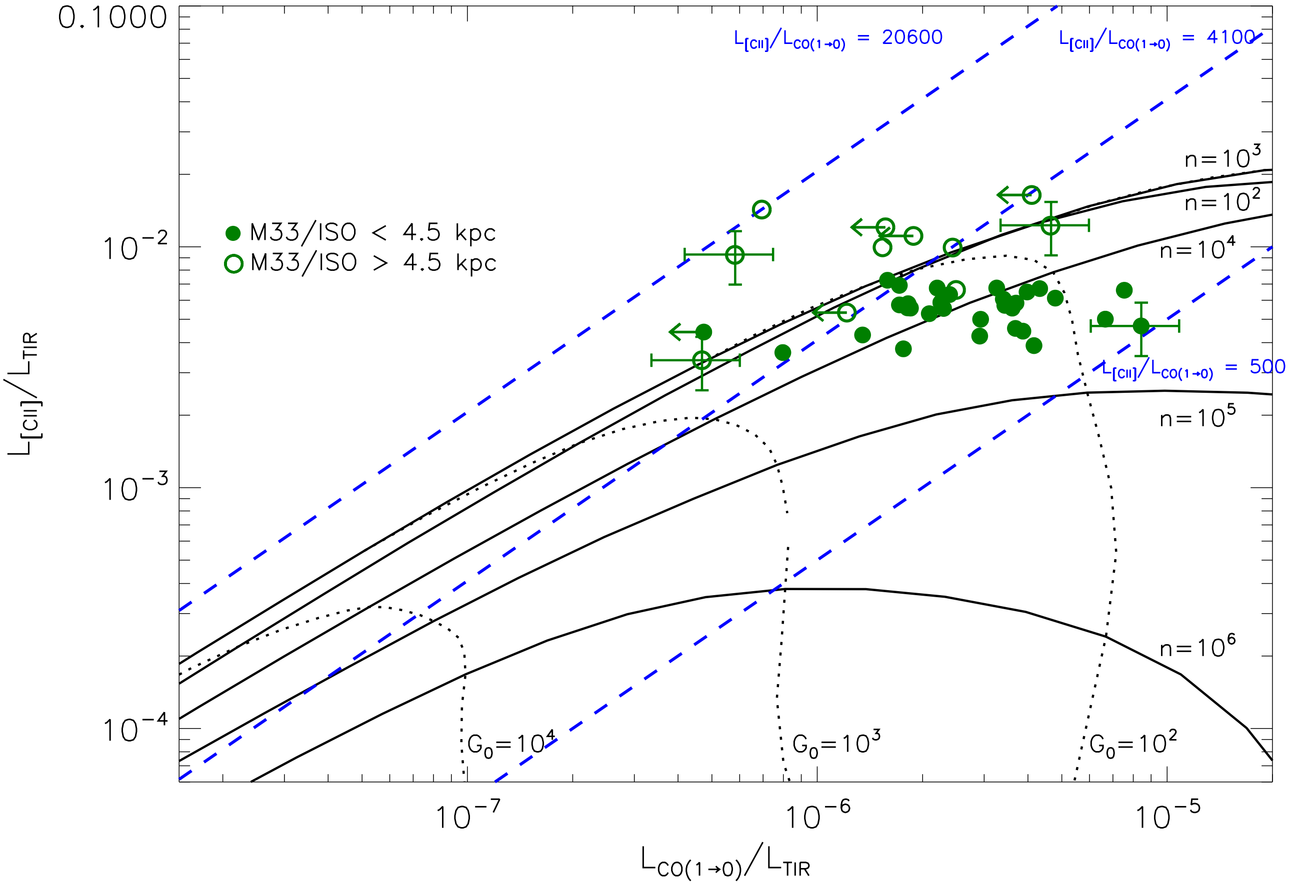

Fig. D.1. [C II] versus CO, which is normalized using the total infrared continuum (TIR). Big green filled circles show ISO/LWS data of the inner S1, N1 regions of M 33, while open circles show data of the outer S2, N2 regions. The lowest [C II]/CO ratio observed with ISO/LWS in M 33 is 1000 (lower blue dashed line), while the highest ratio is 41 200 (upper blue dashed line). Black solid and dotted lines indicate lines of constant density n and FUV field G_0, respectively, from the standard K99 PDR model with A_V = 10 mag and solar metallicity Z = 1.